Structural, Elastic, Vibrational and Electronic Properties of Amorphous Sm_2O_3 from *Ab Initio* Calculations

Emilia Olsson*, Qiong Cai

University of Surrey - Department of Chemical & Process Engineering, Guildford, GU2 7XH, United Kingdom

Jonathon Cottom*, Rasmus Jakobsen, Alexander L. Shluger

University College London - Department of Physics & Astronomy, Gower Street, London, WC1E 6BT, United Kingdom

Abstract

Rare earth oxides have shown great promise in a variety of applications in their own right, and as the building blocks of complex oxides. A great deal of recent interest has been focused on Sm_2O_3, which has shown significant promise as a high-k dielectric and as a ReRAM dielectric. Experimentally, these thin films range from amorphous, through partially crystalline, to poly-crystalline, dependent upon the synthetic conditions. Each case presents a set of modelling challenges that need to be defined and overcome. In this work, the problem of modelling amorphous Sm_2O_3 is tackled, developing an atomistic picture of the effect of amorphization on Sm_2O_3 from a structural and electronic structure perspective.

Keywords: Sm_2O_3, rare earth oxide, sesquioxide, amorphous thin films, non-glass forming amorphous oxides, DFT, structure prediction.

1. Introduction

Rare earth elements play a vital role in a plethora of current and emerging technologies, in applications as diverse as solid oxide fuel cells, through to telecommunications. As a result of this interest, there are an increasing number of technological applications that rely upon rare earth oxides (REO) and the related rare earth complex oxides. The focus of this work, Sm_2O_3, has shown great promise in applications as diverse as a high-k dielectric[1, 2, 3, 4, 5, 6],

*Corresponding authors

Email addresses: k.olsson@surrey.ac.uk (Emilia Olsson*), j.cottom.12@ucl.ac.uk (Jonathon Cottom*)

ReRAM dielectric[7, 8, 9, 10], catalyst[11, 12, 13], sensors[14, 15], and as a dopant in a number of optically important glasses[16, 17, 18].

The most promising electronic device applications for Sm_2O_3 have been found in metal-oxide-semiconductor (MOS) and ReRAM devices.[1, 2, 3, 4, 5, 6, 7, 8, 9, 10] Historically, silicon dioxide (SiO_2) has been employed as a gate oxide layer on silicon substrate for reasons of both performance and ease of processing. The miniaturization of devices has driven the need for high-k dielectrics, physically thicker layers with the same electrical equivalent thickness. This has resulted in the testing of a wide variety of potential high-k gate oxide materials with HfO_2, ZrO_2, SiON, Al_2O_3, La_2O_3, TiO_2, Ta_2O_5, and Y_2O_3 each being considered.[19, 20, 21, 22, 23, 24, 25, 26] This search has led to interest in the REO offering as they do a raft of desirable properties. Sm_2O_3 exhibits a high dielectric constant (up to 15 for the amorphous films[27, 28, 29], and significantly higher in the polycrystalline films[30]), high breakdown electric field (up to 10 MV/cm), large band gap, low leakage current, large conduction band offset with Si, good thermal stability, low frequency dispersion, thermodynamic stability on SiO_2, and low trapping rates.[1, 2] The potential of Sm_2O_3 is clear, however, there are a number of challenges to be overcome before viable Sm_2O_3 devices can be realized.

Sm_2O_3 is typically deployed as a thin film in the above applications, and the structure of these films shows a strong dependence on the substrate, growth conditions, and annealing temperature.[5, 31, 30, 1, 28, 32, 33] In common with a large number of non-glass forming metal oxides, Sm_2O_3 thin films are amorphous as deposited and stable up to a given temperature, above which the poly-crystalline film is observed.[5, 31, 30, 1, 28, 34, 8, 33] The amorphous film is stable below 600°C, with an apparent link between the growth technique and the stability of the amorphous phase.[30, 1, 8, 33] The nature of this relationship is not well understood, although it has been postulated that this is due to the inherent defect concentrations in the films induced by an oxygen deficiency. However, this is far from clear as the available EDX, SIMS, and EELS data describes stoichiometric films.[1, 35, 30, 36, 37, 6, 32, 33] Upon annealing at temperatures greater than 600°C, there is a gradual increase in the degree of crystallization of the film, at temperatures above 900°C the resulting film is entirely poly-crystalline.[30, 1, 35, 6] Stable amorphous films for electronic applications have been successfully produced *via* physical layer deposition (PLD)[30, 33], sputter deposition[8], spin coating[38], and pulse laser deposition[6, 33].

In the crystal phase, Sm_2O_3 can exists in the hexagonal (A-type), monoclinic (B-type), or cubic (C-type) crystal structures. For the lighter lanthanide oxides, the hexagonal phase is favored, whereas the heavier oxides favor the cubic phase. In the case of Sm_2O_3, sitting in the middle of the series, the cubic phase is favored at low temperatures and the monoclinic at high temperatures.[39] Under ambient conditions, the cubic phase is observed, unless during sample preparation high temperatures are employed. In these cases, a mixed cubic-monoclinic phase is formed with the high temperature modifications persisting under ambient conditions. As a result, the films observed are typically cubic or

mixed cubic-monoclinic after annealing.[40]

Electronically, Sm_2O_3 is a wide band gap semiconductor or a narrow band-gap insulator, with a band gap of $\approx$ 5.0 eV, with an experimental range of between 4.70 and 5.10 eV for the crystal[41, 42] and 3 - 4 eV for the amorphous[28]. The band structure of the whole range of lanthanide oxides has attracted a great deal of interest with the $4f$-band forming a localized sub-band in a number of these oxides (Ce, Nb).[41, 28] In Sm_2O_3 the f-band sits within the valence band and the localized $4f$-states are hybridized with the extended oxygen p-states. The complex nature of the electronic structure provides a significant modeling challenge to capture this fine detail.[43] Jiang *et al.*[44, 45], Huang *et al.*[43] and Gillen *et al.*[46] investigated the performance of a range of functionals in describing the electronic structure for the full range of lanthanide oxides. The GW_0, sX-LDA, and HSE06 approaches were shown to best reproduce the experimental results, albeit at a significant computational cost.[46] The two main criteria used to judge functional performance were, firstly, the band gap (absolute and the p-d gap) as this gives a coarse approximation of the ability of a functional to describe the electronic structure of the system. Secondly, the ability of a functional to reproduce the ionic charges, hybridization and position of the localized $4f$ states. In these regards the performance HSE06 and GW_0 well reproduced the experimental results and corrected the incorrect ground states from DFT+U. It was shown that while DFT+U can be tuned to achieve an appropriate description of the band gap, the hybridization of the $4f$ states and the position within the valence and conduction bands remain poorly described.[46] This work guided the choice of functional and gave a robust comparison set before the a-Sm_2O_3 (amorphous Sm_2O_3) structures are considered.

Typically the structure of amorphous materials, both glass forming and non-glass forming, are simulated *via* a molecular dynamics (MD) melt-quench procedure.[47, 48, 49, 50] In the case of glass forming oxides, this approach acts as a reasonable mimic of the experimental glass production process, albeit with a significantly higher cooling rate than achieved experimentally.[51] This approach has been applied to a-SiO_2 more than any other material, with a variety of objectives, such as structure prediction, defect characterization, kinetics of defect processes, and modeling of interfaces with other materials.[52, 53, 54, 55, 56, 57] These approaches have produced structures that have been used to successfully identify defect centers, breakdown mechanisms, and many more atomistic phenomena.[58, 59, 60]

In the case of non-glass forming oxides greater care is needed when producing the amorphous structures *via* a melt-quench to ensure the structures produced represent the systems of interest. The difficulties arise as for these materials the amorphous structures only exist in thin films as the result of strain between oxide and substrate. The structures of these films have successfully been produced *via* the same approach, but the choice of potential and additional validation of the structures produced is required.[61, 62, 63, 64, 65, 66, 67, 68] This extra care is required as the melt-quench procedure is no longer a mimic of the physical process of amorphization.[65, 69] In both cases densities and structure factors derived from X-ray or neutron data are typically used to judge the suitability

of the structures generated.[61, 70, 71] For many technologically important thin films high quality data of this type is not available. Fortunately, there is a wealth of experimental data characterizing a-Sm_2O_3 thin films from numerous experimental perspectives over a number of technological generations. The main techniques employed are XRD, XANES, Raman, FT-IR, dielectric, and TEM measurements. From each of the experimental techniques employed, an insight into the electronic, structural, and mechanical properties of the thin film is gained. These data provide important points of comparison between the models generated *via* the MD melt-quench, and the experimentally observed films and act as a validation set allowing the suitability of the structures produced to be judged and refined.

XRD, ellipsometry and TEM studies confirm the amorphous nature of the films as deposited with no detectable crystal peaks in the XRD or a hint of order in the TEM images.[43, 1, 33] Upon annealing at temperatures above 400 - 600°C, dependant upon growth technique and substrate, the degree of crystalline character increases forming cubic and or monoclinic crystalline regions within the film, which at elevated temperatures > 900°C give the completely poly-crystalline thin film.[6, 72, 30] The picture given by the XRD peaks is further confirmed when the partially crystalline and poly-crystalline films are studied using TEM, showing crystal like islands at the low end of the temperature scale. These structures expand as temperature is increased resulting in the high temperature poly-crystalline films. In addition to HRTEM and XRD Goh *et al.*[1] performed EDX measurements confirming that the stoichiometry of the a-Sm_2O_3 and poly-crystalline thin films are maintained. In addition, Raman spectra of the cubic crystal have principle peaks at 152, 335, 424, and 457 cm^{-1}.[38, 40, 1] For cubic Sm_2O_3, in accordance with group theory, 22 Raman active modes are observed.[40] These peaks are broadened, absent or shifted in the amorphous films. In the polycrystalline films typically the peaks associated with the cubic crystal dominate, with a low concentration of the peaks of monoclinic character.[1]

In this work, we predict the atomic structure of a-Sm_2O_3 and investigate its characteristics. This allows atomistic meaning to be given to the various experimental observations. The calculated and experimental elastic properties, thermal expansion coefficient (TEC), band gap as approximated by the HOMO-LUMO separation, dielectric and vibrational spectra are compared as a test and validation of our model system's ability to capture the properties of the a-Sm_2O_3 films. These models can then be used to study defect and interface effects that are important in the context of Sm_2O_3-based devices.

2. Methodology

The molecular dynamics calculations were conducted using DL_POLY 4,[73] within the NPT ensemble with a Nose-Hoover thermostat and the Cherry *et al.*[74] potential parameterized by Olsson *et al.*[75] based on the general Buckingham potential form. The melts were produced from 80, 270 and 640 atom

Table 1: The effect of cooling rate on the density of the structures produced and the standard deviation associated with each value. The densities generated are all extremely similar in the selected range of cooling rates and cell sizes. The density for cubic crystalline Sm_2O_3 is 8.43 gcm^{-3}.[76]

Cell Size	80 Atoms	270 Atoms	640 Atoms
Cooling Rate Kps^{-1}	ρ (σ) gcm^{-3}	ρ (σ) gcm^{-3}	ρ (σ) gcm^{-3}
1	7.047 (0.088)	7.119 (0.075)	7.131 (0.020)
10	7.046 (0.087)	7.058 (0.082)	7.081 (0.023)
50	7.036 (0.082)	6.935 (0.083)	6.951 (0.029)
100	7.031 (0.079)	6.859 (0.095)	6.923 (0.034)
150	7.015 (0.076)	6.771 (0.085)	6.848 (0.034)
200	7.004 (0.077)	6.707 (0.081)	6.799 (0.064)
Melt	6.083 (0.215)	6.117 (0.093)	5.939 (0.091)

cells of cubic Sm_2O_3. A temperature of 5000 K was found to produce a stable melt, without any void formation. The melt was allowed to equilibrate for 100 ps after which time trajectories were taken at 100 ps intervals and cooled with rates of 1 Kps^{-1}, 10 Kps^{-1}, 50 Kps^{-1}, 100 Kps^{-1}, 150 Kps^{-1} and 200 Kps^{-1} to 1 K. This approach has been shown to be robust for a range of glass forming and non-glass forming oxides, producing disordered structures with the appropriate range and concentration of the structural motifs found in the amorphous thin films. Table 1 shows the density variations as a function of cooling rate, as expected slower cooling rates result in denser structures. The densities generated are all extremely similar although at cooling rates of < 100 Kps^{-1} there is a small increase in density. This increase in density corresponds to the introduction of an increased number of crystal like motifs, matching both the site symmetry and the packing order of the crystal phases, although without a crystal seed to propagate from the orientations are random. As a result the low cooling rates < 100 Kps^{-1} were rejected as they contained both crystalline and amorphous motifs with no clear means of testing whether these inclusions are representative of the partially crystalline Sm_2O_3. By the same token cooling rates > 150 Kps^{-1} introduce melt like structures in low concentrations within the selected cooling rate range. For comparison the crystal density is 8.43 gcm^{-3} meaning all of the structures produced represent a significant reduction in density of amorphization ($\approx 20\%$), in accordance with the shift in coordination (table 2) and in line with the experimental observations.[2]

The 270 atoms cells were found to be structurally converged with respect to coordination number distribution. Therefore the 270 atoms cells were selected and taken forward for production along with a cooling rate of 100 Kps^{-1} being the lowest cooling rate that produces an amorphous structure free of any crystal-like regions. The structural characterization is considered in detail in 3.1.1.

The calculated thermal expansion coefficient for cubic Sm_2O_3 of 8.11×10^{-6} K^{-1} is in good agreement with the experimentally measured TEC value for the cubic phase ($7.5 - 8.8 \times 10^{-6}$ K^{-1}).[77] Hence, the inter-atomic potential set

does well describe the thermal expansion of the studied system.[75]

Density functional theory (DFT) calculations were performed using the Vienna *Ab Initio* Simulation Package (VASP)[78, 79, 80, 81], and the functional selected for the calculations was HSE06[82, 83, 84]. This functional was utilized with a converged plane-wave cutoff of 500 eV and PAW psuedopotentials to describe the core electrons. The PAW psuedopotentials inherently take the scalar relativistic effects into account. The supercells described above were calculated at the Γ-point. The size convergence was tested using a 4x4x4 Γ-centered Monkhorst-Pack k-mesh[85, 86]. From the optimized structures, the dielectric tensor was evaluated utilizing density functional perturbation theory to determine the static dielectric matrix.[87, 88, 89]

Vibrational frequencies were calculated numerically in VASP from the second derivatives of the energy gradient by applying small displacements of the cells in each Cartesian coordinate through the finite difference technique. From the determined Hessian matrix, the elastic tensor consisting of the elastic constants is utilized to determine the mechanical properties of Sm_2O_3. This is obtained by distorting the optimized lattice, so the elastic constants can be calculated from the stress-strain relationships. To save computational effort, only the nonequivalent symmetry displacements are considered. The elastic constants C_{ij} are then calculated from the total energy (E) of the distorted (stressed/strained) simulation cell with volume V from eq. 1.[90, 91]

$$C_{ij} = \frac{1}{V}\frac{\partial^2 E}{\partial \epsilon_i \partial \epsilon_j} \tag{1}$$

with ϵ being the applied strain component. From a general perspective, the elastic constants relates to the material response to a perpendicularly applied pressure to each cell face.[90, 91]

3. Results

3.1. a-Sm_2O_3 Properties

3.1.1. Structural

It is of vital importance during the initial model building to test a series of potentials, cell sizes, and cooling rates to ensure a stable melt coupled to structural convergence is achieved in the final structures.[75] These structures are then validated against the available experimental data ensuring that the structures produced are representative of the systems of interest.

For each of the cell sizes and cooling rates, 10 initial structures are produced. A full description of the structural, physical and elastic properties are included in the supplementary information. In the discussion, the average structures from these ensembles are considered, unless specifically highlighted. Table 2, shows that there is little variation in coordination geometry as a function of cell size with all of the structures showing very similar Sm-coordination, there is a greater distribution of O-coordinations. We note that all of these distributions sit in a tight $\approx 5\%$ range.

Table 2: The average percentage coordination and the associated standard deviation (σ) of Sm and O as a function of cell size to test the size convergence after a DFT cell and geometry optimization.

Sm-Coordination	80 - % (σ)	270 - % (σ)	640 - % (σ)
4	2 (1.4)	2 (0.4)	2 (0.1)
5	39 (2.6)	40 (1.7)	40 (2.0)
6	53 (2.5)	53 (1.6)	53 (1.7)
7	6 (1.3)	4 (0.8)	5 (1)
O-Coordination			
2	7 (5.2)	4 (2.0)	4 (1.5)
3	42 (6.3)	40 (2.4)	41 (2.1)
4	51 (5.0)	56 (2.9)	55 (2.7)

The structures that these coordination distributions relate to are shown for the cubic crystal in Fig. 1, and in Fig. 2 for the amorphous system. In the cubic crystalline phase, each Sm is 6-coordinated in a distorted octahedral configuration with a C_{2h} point symmetry Fig. 1b. The O is 4-coordinated and sits at a distorted tetrahedral site, as shown in Fig. 1c. The high temperature monoclinic phase is based upon a distortion of the cubic crystal introducing 6- and 7-coordinated Sm along with 3- and 4-coordinated O and is included in the supplementary information for completeness.

In the case of the amorphous structures, the single motifs of the crystal structure are replaced by a variety of motifs from 7- to 4-coordinated Sm, and 4- to 2-coordinated O, Fig 2b-e. In addition to the new motifs introduced on amorphization, their mode of tessellation is also modified. In the crystal, all of the 6-coordinated motifs are edge sharing and equivalent, in the case of the amorphous structures a variety of edge and corner sharing connects are introduced (Fig. 2a).

The structures are further analyzed through the calculation of the pair distribution functions for the 80, 270, and 640 atom cells. Table 2 shows negligible variation of atomic coordination as a function of supercell size. For comparison, pair distribution functions for all the individual systems are included in the supplementary material.

The smaller cells show a greater variation as a result of incomplete sampling inherent in the 80 atom cells, these statistical quirks are completely absent in the 270 and 640 atom cells. Fig. 3 shows a comparison between the crystal and the amorphous PDF showing a clear correlation between the crystal and the amorphous peaks. In the amorphous structures these features are spread out compared to the crystal as they describe a variety of structures and distortions inherent in the structure. The components of the total g(r) are shown in Fig. 4 where for each of Sm-O, Sm-Sm, and O-O distributions the sharp peaks of the crystal are broadened and longer range order of the crystal is completely absent.

In addition to the pair distribution functions shown in figures 3, and 4, bond angle distributions are included in the supplementary information for each of

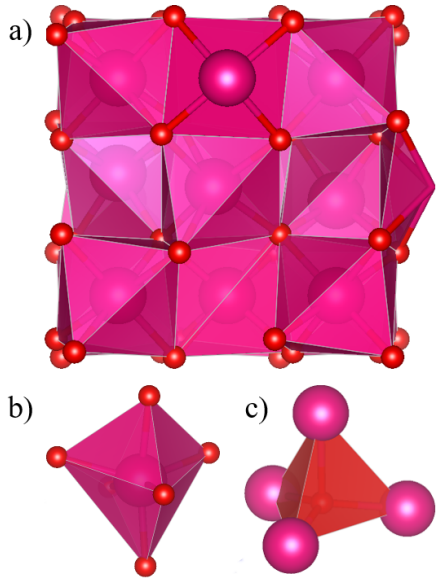

Figure 1: Structure of cubic Sm_2O_3 a) showing the edge sharing distorted octahedral network. b) The 6-coordinated SmO_6 distorted octahedral building block, the distortion of the 6-coordinated centers drops from O_h to C_2. c) The 4-coordinated OSm_4 tetrahedra the distortion to the T_d symmetry is far less pronounced than for the Sm center.[92]

the structures generated along with the ensemble averages.

3.1.2. Elastic and Vibrational Properties

Using the above structures, the elastic and vibrational properties were calculated to facilitate comparison with the available experimental data. Elastic, or mechanical, properties can be directly calculated from the obtained elastic constants as described in the methodology. For low symmetry materials, such as the amorphous oxides investigated here, the bulk (B), shear (G), and Young's (E) moduli can be calculated according to the Voigt formalism from the elastic constants (c_{ij}) eq. 1.[93]

$$B = \frac{1}{9}((c_{11} + c_{22} + c_{33}) + 2(c_{12} + c_{13} + c_{23})) \tag{2}$$

$$G = \frac{1}{15}(c_{11} + c_{22} + c_{33} + 3(c_{44} + c_{55} + c_{66}) - c_{12} - c_{13} - c_{23}) \tag{3}$$

$$E = \frac{9BG}{(3B + G)} \tag{4}$$

The calculated mechanical properties for Sm_2O_3 are summarized in table 3.

The calculated bulk moduli are in good agreement with experimental values obtained from measuring lattice volume at different pressures and then applying

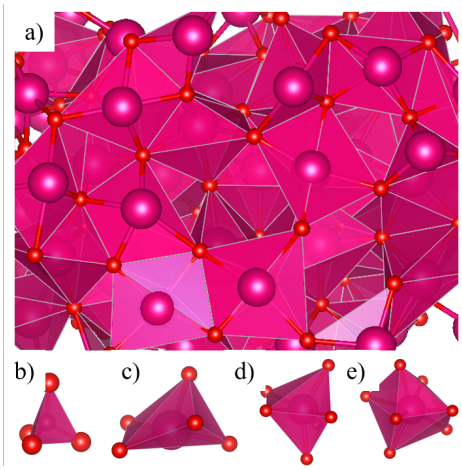

Figure 2: Structure of a-Sm_2O_3 a) showing the disordered array of edge and corner sharing motifs of varying coordination. b) The 4-coordinated SmO_4 distorted tetrahedral building block, based on a relaxation of the under coordinated 6-coordinated crystal center. c) The 5-coordinated SmO_5 unit the distortion and variation is wide enough that consideration of point symmetry far from instructive, d) the 6-coordinated building block based upon the crystal motifs with a range of distortions as a result of the packing environment, e) the 7-coordinated building block represents a distortion of the monoclinic crystalline motif.

the Birch-Murnaghan equation.[40, 35] Examining table 3 it is seen that the values of the mechanical characteristics decrease moving from the cubic crystal to the amorphous. A decrease in B and G values have previously been attributed to a decrease in material hardness and resistance to elastic shear strain. A smaller E is also indicative of a material that is more receptive to physical changes to its structure[90] suggesting that, upon amorphization, Sm_2O_3 becomes more susceptible to structural changes from stress and strain.

Following the elastic properties, the calculated vibrational frequencies were compared to those obtained experimentally for the cubic crystal. As can be seen in figure 6, the here calculated peak positions in the Raman spectra align with the experimental Raman peaks. For the poly-crystalline sample, four major Raman active peaks have been experimentally identified; 152, 335, 424, and 457 cm^{-1}.[38, 40, 1] Furthermore, Amaliroselin *et al*. reported a shallow peak at 528 cm^{-1} for cubic thin films in FT-IR spectra, which was assigned to stretching mode of Sm_2O_3.[38] The same peak can be seen from the simulated vibrational frequencies here at 530 cm^{-1} (Fig. 5). The overall good agreement between the calculated and experimental data for both the Raman active modes and FT-IR modes provides some confidence that the simulation model employed satisfactorily represents Sm_2O_3.

In the amorphous Sm_2O_3 models, a larger spread in vibrational modes is seen with a broadening of the crystal peaks. In addition, broad shallow peaks at $\approx$ 200 cm^{-1} present in the calculated amorphous structures result from the

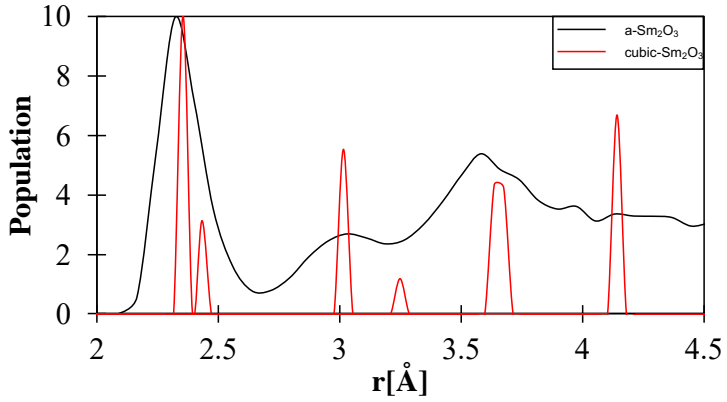

Figure 3: Comparison between the principal peaks of total pair distribution function for the cubic crystal Sm_2O_3 (red line), and the total pair distribution function of a-Sm_2O_3 (black line).

interplay between 6- and 5-coordinated motifs; as there are a broad distribution of geometries the peaks sit across a broad energy range (190 cm^{-1} - 300 cm^{-1}). This accords well with the Raman peaks observed by Goh *et al.*[1] at 245 cm^{-1}. The same study shows that the IR active modes are broadened beyond the point where any signals can be reasonably assigned.

3.1.3. Electronic Properties

The electronic structure calculations were performed using HSE06 as it has been shown to perform well when calculating the hexagonal crystal phase, by Gillan *et al.*[46], and discussed in section 2. Cubic, monoclinic and hexagonal phases of Sm_2O_3 have a measured band gap of 4.9, 4.7, and 5.1 eV, respectively.[41, 42] This is in excellent agreement with the calculated Kohn-Sham band gap values (table 4). In the case of the amorphous phases, there is a marked reduction in band gap from 4.77 eV for the monoclinic structure and 4.91 eV for the cubic structures (Fig. 7), to $\approx$ 3.7 eV for the amorphous systems (table 4). This decrease in insulating character going from crystalline to amorphous phases in binary oxides has previously been seen in Al_2O_3, where the band gap reduction is far more pronounced ($\approx$ 30%).[95, 61] Experimental studies of Sm_2O_3 thin films measure band gaps between 3.15 eV to 4.0 eV[28, 38], with poly-crystalline films showing a larger band gap of 4.0 - 4.6 eV.[1, 30] This is in accordance with the observation of Gillan *et al.* for the hexagonal crystal phase, and has been extended here to the monoclinic (supplementary information) and the cubic phases with the agreement maintained. It should be noted that in the case of the amorphous structures produced, while sitting in the experimental range, the calculated values tend towards the middle-high end of the experimental range. However, both the decrease in band gap and dielectric from crystalline to amorphous are consistent with the experimental work, with

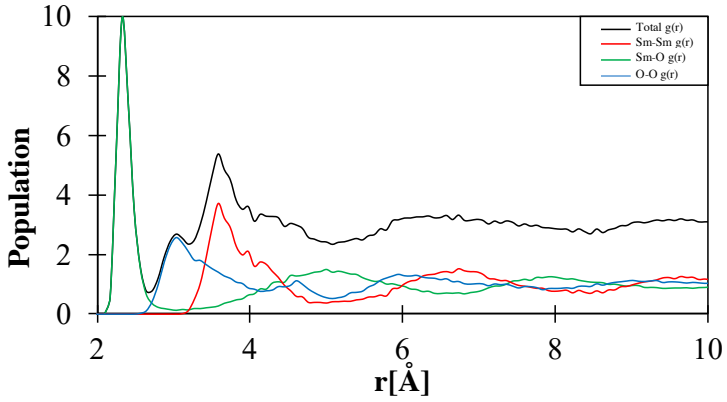

Figure 4: The pair distribution function (g(r)) for a-Sm_2O_3, the black line is the total g(r), the green line is the Sm-O, the red line is the Sm-Sm distribution, and the blue line is the O-O distribution.

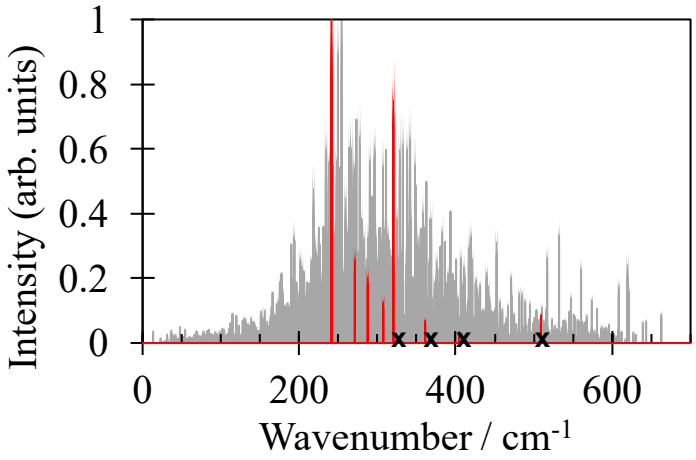

Figure 5: Comparison between the amorphous (grey) and the crystalline (red) IR active modes illustrating the broadening of the crystal features beyond recognition. The amorphous peaks are a combination all of the simulation cells with the individual contributions included in the supplementary material. This helps explain the lack of observable features in the as deposited films and the resultant broad peak. The crosses indicate the experimental peak positions.[40, 38, 92]

all of the calculated values sitting comfortably within the experimental range.

From figure 7 the character of the valence and conduction bands can be seen to be more defined for the crystal than the amorphous phase. The valence band maximum (VBM) of crystalline Sm_2O_3 is composed of O $2p$-states, with hybridization between O p- and Sm f-states seen further down the valence band (≈1 eV below the Fermi level). In the cubic crystal, the valence band is split

Table 3: Calculated bulk moduli (B), shear moduli (G), and Young's moduli (E) for the cubic, and amorphous bulks.

Structure	B (GPa)	G (GPa)	E (GPa)
Cubic	137.26	75.34	191.06
Experimental	130 - 149[40, 35, 90]	-	-
Amorphous			
1	131.65	68.77	175.70
2	129.81	68.16	174.02
3	131.90	70.02	178.48
4	126.73	65.58	167.79
5	133.99	69.53	177.82
6	135.05	71.11	181.49
7	130.82	68.46	174.88
8	130.12	67.61	172.89
9	133.54	69.55	177.79
10	130.75	69.31	176.70

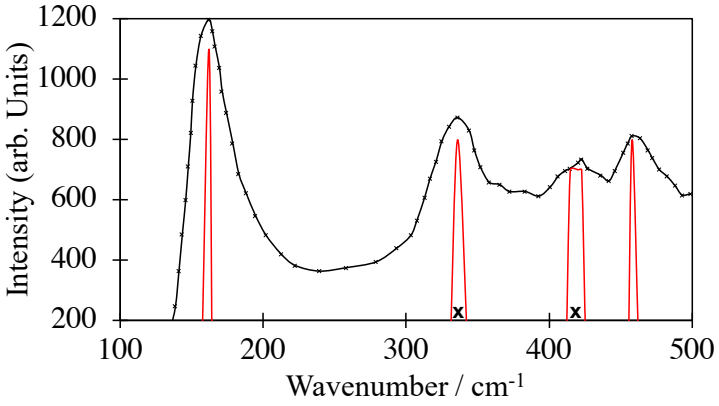

Figure 6: Comparison between the principle peaks of the Raman spectra for the disordered film (black line)[40, 38], and the calculated peak principal peaks (red lines), finally the crosses indicate the single crystal peak positions[94, 92].

into two regions of Sm f-, O p-character near the band edge, and Sm d-, O p-character from ≈ -2 eV below the VBM (Fig. 7a). These clear divisions are smeared out in the amorphous case with contributions from d- and f-states seen across the valence band (Fig. 7b). The conduction band minimum (CBM) shows Sm f-character at the band edge, with d-character from approximately 0.2 eV into the conduction band, as verified in experimental studies[28]. On amorphization, the sharp states are smeared out as a function of distortion and shift in coordination and by extension hybridization. The DOS for each of the structures produced are included in the supplementary information.

Sm_2O_3 has gained attention within the gate dielectric community due to its large band gap and tune-able dielectric properties. Depending on crystal

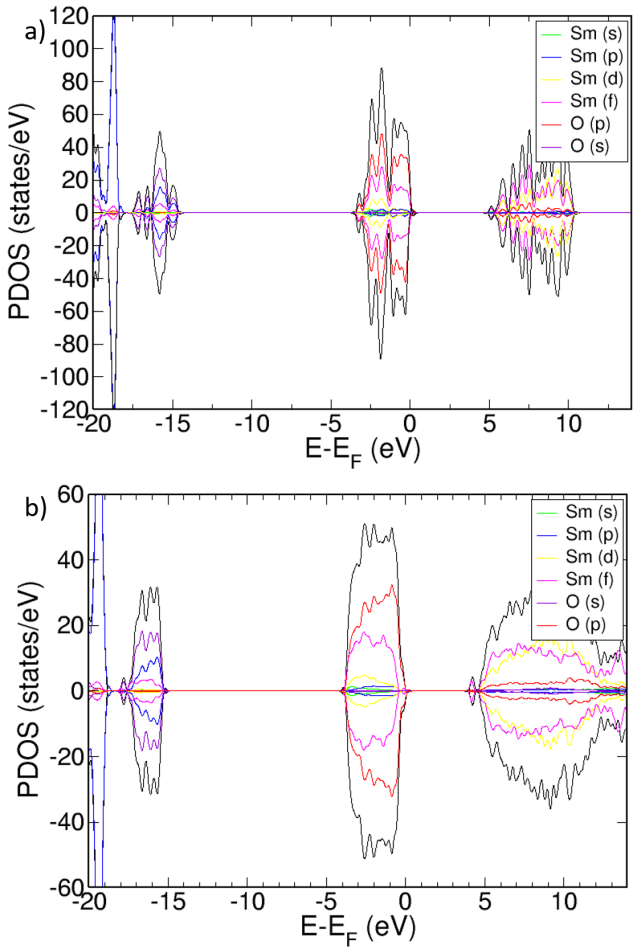

Figure 7: Total and projected density of states for a) cubic, and b) amorphous Sm_2O_3 calculated with HSE06, the DOS is an average of all structures, with the individual contributions included in the supplementary material. Black lines show total density of states, whereas green, blue, yellow, pink, purple, and red are projected density of states.

structure and crystalline character, different experimental dielectric constants (ϵ) have been reported, with higher ϵ indicating a more cubic crystalline character. The calculated dielectric constant for cubic Sm_2O_3 is 30.2, which compares well with the experimentally determined ϵ[96]. Examining the literature, a wide range of ϵ exists, especially for thin films as the ϵ is directly dependent on film thickness, structure, and quality[29, 97, 27]. This spread is clearly seen for the different amorphous bulks modelled here (table 4), which have captured a wide range of the experimentally reported ϵ. This gives confidence that the models produced in this work have reflected the characteristics of the experimentally

synthesized thin films.

Table 4: Calculated band gap (E_g) and dielectric constants (ϵ) for cubic crystal, and the amorphous structures.

Structure	E_g (eV)	ϵ_{xx}	ϵ_{yy}	ϵ_{zz}	ϵ_{mean}
Cubic	4.91	30.2	30.2	30.2	30.2
Experimental[96, 41, 42]	5.0	30.5	30.5	30.5	30.5
Amorphous					
1	3.75	4.28	4.27	4.30	4.28
2	3.63	4.63	5.13	5.83	5.20
3	3.72	4.20	4.24	4.27	4.24
4	3.66	4.22	4.19	4.18	4.20
5	3.85	9.85	9.83	6.68	8.79
6	3.58	7.74	6.94	8.71	7.80
7	3.74	6.60	7.82	5.68	6.70
8	3.64	4.35	4.38	4.36	4.36
9	3.75	6.30	4.57	7.78	6.22
10	3.70	4.32	4.28	4.31	4.30
Experimental[28, 29, 27]	3.15-3.9	-	-	-	4 - 11

4. Conclusion

The method for preparing a-Sm_2O_3 models presented here provides robust means of model generation and validation to allow the study of a-Sm_2O_3. This approach ensures that the available experimental data, both structural and electronic, are tested against the models produced, hence directly applicable to the system of study. This is not to suggest that there are not still challenges remaining from a structural perspective, the models produced in this work relate to the low temperature regime $< 600^{\circ}$C where the produced films are clearly amorphous. At higher temperatures, 600°C - 900°C, the produced films have characteristics of both the crystalline and amorphous, and are typically viewed as being made up of crystalline domains linked by disordered regions. These features are not captured by the amorphous systems presented and present a formidable modeling challenge.

The calculated elastic properties show excellent agreement with the crystalline and the amorphous structures. The shift in coordination and the evolution of the point symmetry associated with each of the structural motifs gives a level of detail that is impossible to obtain by other means. This presents a picture of 6-coordinated Sm in the cubic crystal phase, and 4-coordinated O in the crystal phase are replaced by a range of coordinations. With 4-, 5-, 6-, and 7-coordinated Sm, and 2-, 3-, and 4-coordinated O, within each of these coordination environments a variety of symmetry groups are accessible along with their distorted variants. Direct consideration of the point groups associated with these coordination environments is not particularly illuminating, as would

be the case in the crystal, given the large variation and inherent distortions in the motifs. These variations are a result of the local steric packing and gives rise to a range of Sm-O bond length (and angles) centered around the crystal value.

The change in coordination has a dramatic effect on the observed vibrational spectra with a smearing out of the strong features observed in the cubic crystal, peaks at 152, 345, and 424 cm^{-1}, and the introduction of broad features at $\approx$ 200 cm^{-1} that are absent in any of the crystal phases. The elastic properties, bulk modulus, shear modulus, and Young's modulus, all show a small reduction when compared to the cubic crystal phase. This is in good agreement with the observed softening in the amorphous as deposited films.

The structural modifications on amorphization have a marked effect on the electronic structure of the thin films when compared to the crystal phases. This is observed in a significant contraction ($\approx$ 24 %) of the HOMO - LUMO separation when compared with the crystal phase. This is the result of a reduction in density on amorphization and a change in hybridization. These two effects together lead to the observed contraction in the HOMO-LUMO separation. With 5-coordinated Sm-states introduced at the CBM, inside the 6-coordinated states, by the same token 2- and 3-coordinated O states are introduced at the VBM. Further study is required to confirm how this change in electronic structure on amorphization effects the performance of Sm_2O_3 as a gate dielectric and the observation of intrinsic charge trapping and the performance limitation inherent with this behaviour. The structures generated show excellent agreement with the available experimental results and allow an atomistic understanding of a-Sm_2O_3 to be developed.

5. Data Availability Statement

The raw data required to reproduce these findings are available from the authors on request. The processed data required to reproduce these findings is provided in the electronic supplementary material.

6. Acknowledgements

EO and QC would like to acknowledge the financial support from EPSRC (Engineering and Physical Sciences Council) under grant number EP/R021554/1. JC and ALS acknowledge the Leverhulme Trust (RPG-2016-135). Computational resources on Archer (http://www.archer.ac.uk) were provided via our membership of the UK's HEC Materials Chemistry Consortium, which is funded by EPSRC (EP/L000202). The authors would like to thank Stephan Lany, David Mora-Fonz, and Jack Strand for illuminating discussions on the nature of disorder and amorphization.

References

[1] K. H. Goh, A. S. M. A. Haseeb, Y. H. Wong, Effect of Oxidation Temperature on Physical and Electrical Properties of Sm2O3 Thin-Film Gate Oxide on Si Substrate, Journal of Electronic Materials 45 (10) (2016) 5302–5312. doi:10.1007/s11664-016-4694-z.
URL http://link.springer.com/10.1007/s11664-016-4694-z

[2] K. H. Goh, A. S. Haseeb, Y. H. Wong, Lanthanide rare earth oxide thin film as an alternative gate oxide, Materials Science in Semiconductor Processing 68 (2017) 302–315. doi:10.1016/j.mssp.2017.06.037.

[3] S. Kitai, O. Maida, T. Kanashima, M. Okuyama, Preparation and Characterization of High- ¡i¿k¡/i¿Praseodymium and Lanthanoid Oxide Thin Films Prepared by Pulsed Laser Deposition, Japanese Journal of Applied Physics 42 (Part 1, No. 1) (2003) 247–253. doi:10.1143/JJAP.42.247.
URL http://stacks.iop.org/1347-4065/42/247

[4] V. Rozhkov, A. Trusova, I. G. Berezhnoy, Silicon MIS structures using samarium oxide films, Thin Solid Films 325 (1-2) (1998) 151–155. doi:10.1016/S0040-6090(98)00533-1.

[5] W. C. Chin, K. Y. Cheong, Z. Hassan, Sm2O3gate dielectric on Si substrate (2010). doi:10.1016/j.mssp.2011.02.001.
URL http://dx.doi.org/10.1016/j.mssp.2011.02.001

[6] G. H. Chen, Z. F. Hou, X. G. Gong, Density functional calculations on atomic and electronic structures of amorphous HfO[sub 2]/Si(001) interface, Applied Physics Letters 95 (10) (2009) 102905. doi:10.1063/1.3226636.
URL http://link.aip.org/link/APPLAB/v95/i10/p102905/s1&Agg=doi

[7] S. Mondal, C. H. Chueh, T. M. Pan, High-performance flexible Ni Sm2 O3 ITO ReRAM device for low-power nonvolatile memory applications, IEEE Electron Device Letters 34 (9) (2013) 1145–1147. doi:10.1109/LED.2013.2272455.

[8] S. Mondal, C. H. Chueh, T. M. Pan, Current conduction and resistive switching characteristics of Sm 2O3 and Lu2O3 thin films for low-power flexible memory applications, Journal of Applied Physics 115 (1) (2014) 014501. doi:10.1063/1.4858417.

[9] J.-Y. Lin, K.-Y. Wu, K.-H. Chen, C.-M. Cheng, C.-Y. Li, Bipolar switching properties of bilayer V¡inf¿2¡/inf¿O¡inf¿5¡/inf¿/Sm¡inf¿2¡/inf¿O¡inf¿3¡/inf¿thin-film resistive random access memory device prepared by sputtering technology, Sensors and Materials 30 (4) (2018) 933–938. doi:10.18494/SAM.2018.1796.

[10] S.-Y. Huang, T.-C. Chang, M.-C. Chen, S.-C. Chen, H.-P. Lo, H.-C. Huang, D.-S. Gan, S. M. Sze, M.-J. Tsai, Resistive switching characteristics of Sm2O3 thin films for nonvolatile memory applications, Solid-State Electronics 63 (1) (2011) 189–191. doi:DOI:10.1016/j.sse.2011.04.012.
URL http://www.sciencedirect.com/science/article/pii/S0038110111001341

[11] H. X. Dai, C. F. Ng, C. T. Au, Raman spectroscopic and EPR investigations of oxygen species on SrCl 2 -promoted Ln 2 O 3 (Ln = Sm and Nd) catalysts for ethane-selective oxidation to ethene, Applied Catalysis A 202 (2000) 1–15.

[12] M. J. Capitan, P. Malet, M. A. Centeno, A. Munoz-Paez, I. Carrizosa, J. A. Odriozola, Samarium oxide (Sm2O3)/alumina catalysts for methane coupling. Influence of the structure of surface samarium-aluminum-oxygen phases on the reactivity, The Journal of Physical Chemistry 97 (36) (1993) 9233–9240. doi:10.1021/j100138a027.
URL http://pubs.acs.org/doi/abs/10.1021/j100138a027

[13] Z. Taherian, M. Yousefpour, M. Tajally, B. Khoshandam, A comparative study of ZrO2, Y2O3and Sm2O3promoted Ni/SBA-15 catalysts for evaluation of CO2/methane reforming performance, International Journal of Hydrogen Energy 42 (26) (2017) 16408–16420. doi:10.1016/j.ijhydene.2017.05.095.
URL http://dx.doi.org/10.1016/j.ijhydene.2017.05.095

[14] C. R. Michel, A. H. Martínez-Preciado, R. Parra, C. M. Aldao, M. A. Ponce, Novel CO2and CO gas sensor based on nanostructured Sm2O3hollow microspheres, Sensors and Actuators, B: Chemical 202 (2014) 1220–1228. doi:10.1016/j.snb.2014.06.038.
URL http://dx.doi.org/10.1016/j.snb.2014.06.038

[15] M. H. Wu, C. H. Cheng, C. S. Lai, T. M. Pan, Structural properties and sensing performance of high-k Sm2O3membrane-based electrolyte-insulator-semiconductor for pH and urea detection, Sensors and Actuators, B: Chemical 138 (1) (2009) 221–227. doi:10.1016/j.snb.2009.01.059.

[16] S. Y. El-Zaiat, M. B. El-Den, S. U. El-Kameesy, Y. A. El-Gammam, Spectral dispersion of linear optical properties for Sm2O3doped B2O3PbOAl2O3glasses, Optics and Laser Technology 44 (5) (2012) 1270–1276. doi:10.1016/j.optlastec.2011.12.051.
URL http://dx.doi.org/10.1016/j.optlastec.2011.12.051

[17] N. Yaru, L. Chunhua, Z. Yan, Z. Qitu, X. Zhongzi, Study on Optical Properties and Structure of Sm2O3Doped Boron-Aluminosilicate Glass, Journal of Rare Earths 25 (SUPPL. 1) (2007) 94–98. doi:10.1016/S1002-0721(07)60532-8.

[18] J. M. Park, H. J. Kim, S. Kim, P. Limsuwan, J. Kaewkhao, Luminescence property of rare-earth doped bismuth-borate glasses, Procedia Engineering 32 (2012) 855–861. doi:10.1016/j.proeng.2012.02.023.
URL http://dx.doi.org/10.1016/j.proeng.2012.02.023

[19] G. D. Wilk, R. M. Wallace, J. M. Anthony, High-κ gate dielectrics: Current status and materials properties considerations, Journal of Applied Physics 89 (10) (2001) 5243–5275. doi:10.1063/1.1361065.

[20] Y. H. Wong, K. Y. Cheong, ZrO2thin films on Si substrate, Journal of Materials Science: Materials in Electronics 21 (10) (2010) 980–993. doi:10.1007/s10854-010-0144-5.

[21] S. I. Ohmi, C. Kobayashi, K. Aizawa, S. Yamamoto, E. Tokumitsu, H. Ishiwara, H. Iwai, High quality ultrathin La2O3films for high-k gate insulator, in: European Solid-State Device Research Conference, 2001, pp. 235–238. doi:10.1109/ESSDERC.2001.195244.

[22] Y. Kim, S. I. Ohmi, K. Tsutsui, H. Iwai, Space-charge-limited currents in la2O3 thin films deposited by E-beam evaporation after low temperature dry-nitrogen annealing, Japanese Journal of Applied Physics, Part 1: Regular Papers and Short Notes and Review Papers 44 (6 A) (2005) 4032–4042. doi:10.1143/JJAP.44.4032.

[23] C. C. Chew, K. H. Goh, M. S. Gorji, C. G. Tan, S. Ramesh, Y. H. Wong, Breakdown field enhancement of Si-based MOS capacitor by post-deposition annealing of the reactive sputtered ZrOxNygate oxide, Applied Physics A: Materials Science and Processing 122 (2) (2016) 1–6. doi:10.1007/s00339-016-9624-7.

[24] V. V. Afanas'ev, A. Stesmans, F. Chen, X. Shi, S. A. Campbell, Internal photoemission of electrons and holes from (100)Si into HfO2, Applied Physics Letters 81 (6) (2002) 1053–1055. doi:10.1063/1.1495088.

[25] J. Päiväsaari, M. Putkonen, L. Niinistö, A comparative study on lanthanide oxide thin films grown by atomic layer deposition, Thin Solid Films 472 (1-2) (2005) 275–281. doi:10.1016/j.tsf.2004.06.160.

[26] L. Shi, Y. Yuan, X. F. Liang, Y. D. Xia, J. Yin, Z. G. Liu, Microstructure and dielectric properties of La2O3doped amorphous SiO2films as gate dielectric material, Applied Surface Science 253 (7) (2007) 3731–3735. doi:10.1016/j.apsusc.2006.08.006.

[27] A. A. Atta, M. M. El-Nahass, K. M. Elsabawy, M. M. Abd El-Raheem, A. M. Hassanien, A. Alhuthali, A. Badawi, A. Merazga, Optical characteristics of transparent samarium oxide thin films deposited by the radio-frequency sputtering technique, Pramana - Journal of Physics 87 (5) (2016) 1–8. doi:10.1007/s12043-016-1285-8.

[28] W. C. Chin, K. Y. Cheong, Z. Hassan, Sm2O3 gate dielectric on Si substrate, Materials Science in Semiconductor Processing 13 (5-6) (2010) 303–314. doi:10.1016/j.mssp.2011.02.001.

[29] F. H. Chen, M. N. Hung, J. F. Yang, S. Y. Kuo, J. L. Her, Y. H. Matsuda, T. M. Pan, Effect of surface roughness on electrical characteristics in amorphous InGaZnO thin-film transistors with high-κ Sm2O3dielectrics, Journal of Physics and Chemistry of Solids 74 (4) (2013) 570–574. doi:10.1016/j.jpcs.2012.12.006.
URL http://dx.doi.org/10.1016/j.jpcs.2012.12.006

[30] A. A. Dakhel, Dielectric and optical properties of samarium oxide thin films, Journal of Alloys and Compounds 365 (1-2) (2004) 233–239. doi:10.1016/S0925-8388(03)00615-7.

[31] L. Yin, D. Wang, J. Huang, G. Tan, H. Ren, Controllable synthesis of Sm2O3 crystallites with the assistance of templates by a hydrothermal-calcination process, Materials Science in Semiconductor Processing 30 (2015) 9–13. doi:10.1016/j.mssp.2014.09.034.
URL http://dx.doi.org/10.1016/j.mssp.2014.09.034

[32] T. M. Pan, C. C. Huang, Effects of oxygen content and postdeposition annealing on the physical and electrical properties of thin Sm2O3 gate dielectrics, Applied Surface Science 256 (23) (2010) 7186–7193. doi:10.1016/j.apsusc.2010.05.048.

[33] C. Constantinescu, V. Ion, A. C. Galca, M. Dinescu, Morphological, optical and electrical properties of samarium oxide thin films, Thin Solid Films 520 (20) (2012) 6393–6397. doi:10.1016/j.tsf.2012.06.049.
URL http://dx.doi.org/10.1016/j.tsf.2012.06.049

[34] D. Yang, L. J. Xue, R. A. B. Devine, Charge trapping in and electrical properties of pulsed laser deposited Sm2O3 films, Journal of Applied Physics 93 (11) (2003) 9389–9391. doi:10.1063/1.1569660.
URL http://aip.scitation.org/doi/10.1063/1.1569660

[35] Q. Guo, Y. Zhao, C. Jiang, W. L. Mao, Z. Wang, Phase transformation in Sm2O3 at high pressure: In situ synchrotron X-ray diffraction study and ab initio DFT calculation, Solid State Communications 145 (5-6) (2008) 250–254. doi:10.1016/j.ssc.2007.11.019.
URL http://linkinghub.elsevier.com/retrieve/pii/S0038109807008150

[36] X. D. Huang, P. T. Lai, L. Liu, J. P. Xu, Nitrided SrTiO[sub 3] as charge-trapping layer for nonvolatile memory applications, Applied Physics Letters 98 (24) (2011) 242905. doi:10.1063/1.3601473.
URL http://scitation.aip.org/content/aip/journal/apl/98/24/10.1063/1.3601473

[37] T.-M. Pan, C.-C. Huang, S.-X. You, C.-C. Yeh, Effect of Annealing on the Structural and Electrical Properties of High-k Sm[sub 2]O[sub 3] Dielectrics, Electrochemical and Solid-State Letters 11 (12) (2008) G62. doi:10.1149/1.2990226.
URL http://esl.ecsdl.org/cgi/doi/10.1149/1.2990226

[38] A. Amaliroselin, N. Anandhan, G. Ravi, M. Mummoorthi, T. Marimuthu, Growth and characterization of Sm 2 O 3 thin films by spin coating technique, International Journal of ChemTech Research 6 (13) (2014) 5315–5320. doi:10.1016/j.apcatb.2004.11.022.

[39] S. C. Atkinson, Crystal Structures and Phase Transitions in the Rare Earth Oxides, PhD Thesis (July) (2013) 1–236.

[40] S. Jiang, J. Liu, C. Lin, X. Li, Y. Li, High-pressure x-ray diffraction and Raman spectroscopy of phase transitions in Sm2O3, Journal of Applied Physics 113 (11) (2013) 1–7. doi:10.1063/1.4795504.

[41] A. Prokofiev, A. Shelykh, B. Melekh, Periodicity in the band gap variation of Ln2X3 (X = O, S, Se) in the lanthanide series, Journal of Alloys and Compounds 242 (1-2) (1996) 41–44. doi:10.1016/0925-8388(96)02293-1.
URL http://www.sciencedirect.com/science/article/pii/0925838896022931

[42] L. Petit, A. Svane, Z. Szotek, W. M. Temmerman, O. Ce, First-principles study of rare-earth oxides, Physical Review B 72 (205118) (2005) 1–9. doi:10.1103/PhysRevB.72.205118.

[43] B. Huang, 4F Fine-Structure Levels As the Dominant Error in the Electronic Structures of Binary Lanthanide Oxides, Journal of Computational Chemistry 37 (9) (2016) 825–835. doi:10.1002/jcc.24272.

[44] H. Jiang, P. Rinke, M. Scheffler, Electronic properties of lanthanide oxides from the GW perspective, Physical Review B - Condensed Matter and Materials Physics 86 (12) (2012) 1–13. doi:10.1103/PhysRevB.86.125115.

[45] H. Jiang, R. I. Gomez-abal, P. Rinke, M. Scheffler, Localized and Itinerant States in Lanthanide Oxides United by GW @ LDA U, Phyiscal Review Letters 126403 (March) (2009) 1–4. doi:10.1103/PhysRevLett.102.126403.

[46] R. Gillen, S. J. Clark, J. Robertson, Nature of the electronic band gap in lanthanide oxides, Physical Review B - Condensed Matter and Materials Physics 87 (12) (2013) 1–6. doi:10.1103/PhysRevB.87.125116.

[47] S. von Alfthan, A. Kuronen, K. Kaski, Realistic models of amorphous silica: A comparative study of different potentials, Phys. Rev. B 68 (7) (2003) 73203. doi:10.1103/PhysRevB.68.073203.
URL https://link.aps.org/doi/10.1103/PhysRevB.68.073203

[48] K. Vollmayr, W. Kob, K. Binder, Cooling-rate effects in amorphous silica: A computer-simulation study, Phys. Rev. B 54 (22) (1996) 15808–15827. doi:10.1103/PhysRevB.54.15808.
URL https://link.aps.org/doi/10.1103/PhysRevB.54.15808

[49] S. Mukhopadhyay, P. Sushko, A. Stoneham, A. L. Shluger, Modeling of the structure and properties of oxygen vacancies in amorphous silica, Physical Review B 70 (19) (2004) 195203. doi:10.1103/PhysRevB.70.195203.
URL http://link.aps.org/doi/10.1103/PhysRevB.70.195203

[50] B. W. H. van Beest, G. J. Kramer, R. A. van Santen, Force fields for silicas and aluminophosphates based on ab initio calculations, Physical Review Letters 64 (16) (1990) 1955–1958. doi:10.1103/PhysRevLett.64.1955.
URL https://link.aps.org/doi/10.1103/PhysRevLett.64.1955

[51] M. Ivanda, D. Ristić, M. Ferrari, G. Speranza, Quantifying inhomogeneities in silicon-rich oxide thin films, SPIE Newsroom (2013) 2–4doi:10.1117/2.1201303.004785.
URL http://www.spie.org/x93485.xml

[52] S. Ling, A. M. El-Sayed, F. Lopez-Gejo, M. B. Watkins, V. V. Afanas'ev, A. L. Shluger, A computational study of Si–H bonds as precursors for neutral E' centres in amorphous silica and at the Si/SiO2 interface, Microelectronic Engineering 109 (2013) 310–313. doi:10.1016/j.mee.2013.03.028.
URL http://dx.doi.org/10.1016/j.mee.2013.03.028

[53] A.-M. El-Sayed, M. B. Watkins, V. V. Afanas'ev, A. L. Shluger, Nature of intrinsic and extrinsic electron trapping in SiO2, Physical Review B 89 (12) (2014) 125201. doi:10.1103/PhysRevB.89.125201.
URL http://link.aps.org/doi/10.1103/PhysRevB.89.125201

[54] M. S. Munde, D. Z. Gao, A. L. Shluger, Diffusion and aggregation of oxygen vacancies in amorphous silica, Journal of Physics Condensed Matter 29 (24) (2017) 245701. doi:10.1088/1361-648X/aa6f9a.

[55] S. Mukhopadhyay, P. V. Sushko, V. A. Mashkov, A. L. Shluger, Spectroscopic features of dimer and dangling bond E centres in amorphous silica, J. Phys.: Condens. Matter 17 (2005) 1311–1318. doi:10.1088/0953-8984/17/8/009.
URL http://iopscience.iop.org/0953-8984/17/8/009

[56] A. Stirling, A. Pasquarello, Modelling of paramagnetic trivalent silicon defect centres in amorphous silica and at Si–SiO 2 interfaces, Journal of Physics: Condensed Matter 17 (21) (2005) S2099–S2113. doi:10.1088/0953-8984/17/21/006.
URL http://stacks.iop.org/0953-8984/17/i=21/a=006?key=crossref.1c97c1fe6100f86d88eec0e7de83b8e5

[57] F. Devynck, A. Alkauskas, P. Broqvist, A. Pasquarello, Charge transition levels of carbon-, oxygen-, and hydrogen-related defects at the SiC/SiO2 interface through hybrid functionals, Physical Review B 84 (23) (2011) 235320. doi:10.1103/PhysRevB.84.235320.
URL http://link.aps.org/doi/10.1103/PhysRevB.84.235320

[58] J. Cottom, G. Gruber, G. Pobegen, T. Aichinger, A. L. Shluger, Recombination defects at the 4H-SiC/SiO ¡sub¿2¡/sub¿ interface investigated with electrically detected magnetic resonance and ¡i¿ab initio¡/i¿ calculations, Journal of Applied Physics 124 (4) (2018) 045302. doi:10.1063/1.5024608.
URL http://aip.scitation.org/doi/10.1063/1.5024608

[59] Y. Wimmer, A.-M. El-Sayed, W. Gös, T. Grasser, A. L. Shluger, Role of hydrogen in volatile behaviour of defects in SiO ¡sub¿2¡/sub¿ -based electronic devices, Proceedings of the Royal Society A: Mathematical, Physical and Engineering Science 472 (2190) (2016) 20160009. doi:10.1098/rspa.2016.0009.
URL http://rspa.royalsocietypublishing.org/lookup/doi/10.1098/rspa.2016.0009

[60] D. Z. Gao, A.-M. El-Sayed, A. L. Shluger, Structure and properties of defects in amorphous silica A mechanism for Frenkel defect creation in amorphous SiO 2 facilitated by electron injection, Nanotechnology 27 (50) (2016) 505207.

[61] O. A. Dicks, A. L. Shluger, Theoretical modeling of charge trapping in crystalline and amorphous Al 2 O 3, Journal of Physics: Condensed Matter 29 (31) (2017) 314005. doi:10.1088/1361-648X/aa7767.
URL http://iopscience.iop.org/article/10.1088/1361-648X/aa7767/pdf%0Ahttp://stacks.iop.org/0953-8984/29/i=31/a=314005?key=crossref.5f790ab460f0691e5347d73832091481

[62] J. Strand, O. A. Dicks, M. Kaviani, A. L. Shluger, Hole trapping in amorphous HfO2and Al2O3as a source of positive charging, Microelectronic Engineering 178 (2017) 235–239. doi:10.1016/j.mee.2017.05.012.
URL http://dx.doi.org/10.1016/j.mee.2017.05.012

[63] M. Kaviani, J. Strand, V. V. Afanas'Ev, A. L. Shluger, Deep electron and hole polarons and bipolarons in amorphous oxide, Physical Review B 94 (2) (2016) 020103. doi:10.1103/PhysRevB.94.020103.

[64] J. Strand, M. Kaviani, D. Gao, A.-M. El-Sayed, V. Afanas'Ev, A. Shluger, Intrinsic charge trapping in amorphous oxide films: Status and challenges, Journal of Physics Condensed Matter 30 (23) (2018) 2330001. doi:10.1088/1361-648X/aac005.

[65] D. B. Buchholz, Q. Ma, D. Alducin, A. Ponce, M. Jose-Yacaman, R. Khanal, J. E. Medvedeva, R. P. H. Chang, The Structure and Properties of Amorphous Indium Oxide., Chemistry of materials : a publication of the American Chemical Society 26 (18) (2014) 5401–5411. doi:10.1021/cm502689x.
URL http://dx.doi.org/10.1021/cm502689x

[66] L. C. Gallington, Y. Ghadar, L. B. Skinner, J. K. Weber, S. V. Ushakov, A. Navrotsky, A. Vazquez-Mayagoitia, J. C. Neuefeind, M. Stan, J. J. Low, C. J. Benmore, The structure of liquid and amorphous hafnia, Materials 10 (11) (2017) 1290. doi:10.3390/ma10111290.

[67] Z. Guo, F. Ambrosio, A. Pasquarello, Oxygen defects in amorphous Al2O3: A hybrid functional study, Applied Physics Letters 109 (6) (2016) 0–4. doi:10.1063/1.4961125.

[68] Y. Wang, F. Zahid, J. Wang, H. Guo, Structure and dielectric properties of amorphous high-κ oxides: HfO 2, ZrO 2, and their alloys, Physical Review B - Condensed Matter and Materials Physics 85 (22) (2012) 1–5. doi:10.1103/PhysRevB.85.224110.

[69] J. Mavračić, F. C. Mocanu, V. L. Deringer, G. Csányi, S. R. Elliott, Similarity between Amorphous and Crystalline Phases: The Case of TiO2, Journal of Physical Chemistry Letters 9 (11) (2018) 2985–2990. doi:10.1021/acs.jpclett.8b01067.

[70] B. Shyam, K. H. Stone, R. Bassiri, M. M. Fejer, M. F. Toney, A. Mehta, Measurement and Modeling of Short and Medium Range Order in Amorphous Ta2O5 Thin Films, Scientific Reports 6 (1) (2016) 32170. doi:10.1038/srep32170.
URL http://www.nature.com/articles/srep32170

[71] N. Kim, R. Bassiri, M. M. Fejer, J. F. Stebbins, The structure of ion beam sputtered amorphous alumina films and effects of Zn doping: High-resolution27Al NMR, Journal of Non-Crystalline Solids 405 (2014) 1–6. doi:10.1016/j.jnoncrysol.2014.08.022.
URL http://dx.doi.org/10.1016/j.jnoncrysol.2014.08.022

[72] T.-J. Chen, C.-L. Kuo, Oxygen vacancy formation and the induced defect states in HfO2 and Hf-silicates – A first principles hybrid functional study, Microelectronics Reliability 54 (6-7) (2014) 1119–1124. doi:10.1016/j.microrel.2013.10.013.
URL http://www.sciencedirect.com/science/article/pii/S0026271413003958

[73] I. T. Todorov, W. Smith, K. Trachenko, M. T. Dove, DL_POLY, Journal of Materials Chemistry 16 (2006) 1911–1918.
URL http://www.ccp5.ac.uk/DL_POLY/

[74] M. Cherry, M. S. Islam, C. R. A. Catlow, Oxygen ion migration in perovskite-type oxides, Journal of Solid State Chemistry 118 (1995) 125–132.
URL http://www.sciencedirect.com/science/article/pii/S0022459685713205

[75] E. Olsson, X. Aparicio-Anglès, N. H. De Leeuw, A computational study of the electronic properties, ionic conduction, and thermal expansion of Sm¡inf¿1-x¡/inf¿A¡inf¿x¡/inf¿CoO¡inf¿3¡/inf¿and Sm¡inf¿1-x¡/inf¿A¡inf¿x¡/inf¿CoO¡inf¿3-x/2¡/inf¿(A = Ba¡sup¿2+¡/sup¿, Ca¡sup¿2+¡/sup¿, Sr¡sup¿2+¡/sup¿, and x =, Physical Chemistry Chemical Physics 19 (21) (2017) 13960–13969. doi:10.1039/c7cp01555k.

[76] B. T. Sone, E. Manikandan, A. Gurib-Fakim, M. Maaza, Sm¡inf¿2¡/inf¿O¡inf¿3¡/inf¿ nanoparticles green synthesis via Callistemon viminalis' extract, Journal of Alloys and Compounds 650 (2015) 357–362. doi:10.1016/j.jallcom.2015.07.272.
URL http://dx.doi.org/10.1016/j.jallcom.2015.07.272

[77] S. Stecura, W. J. Campbell, Thermal expansion and phase inversion of rare-earth oxides, US Bureau of Mines Report Number 5847 (1961) 1–46doi:10.2172/4840970.
URL https://doi.org/10.2172/4840970

[78] G. Kresse, J. Hafner, Ab initio molecular dynamics for liquid metals, Physical Review B 47 (1) (1993) 558–561. doi:10.1103/PhysRevB.47.558.

[79] G. Kresse, J. Hafner, Ab initio molecular-dynamics simulation of the liquid-metal–amorphous-semiconductor transition in germanium, Physical Review B 49 (20) (1994) 14251–14269. doi:10.1103/PhysRevB.49.14251.
URL http://link.aps.org/doi/10.1103/PhysRevB.49.14251

[80] G. Kresse, J. Furthmüller, Efficiency of ab-initio total energy calculations for metals and semiconductors using a plane-wave basis set, Computational Materials Science 6 (1) (1996) 15–50. doi:10.1016/0927-0256(96)00008-0.
URL http://www.sciencedirect.com/science/article/pii/0927025696000080

[81] G. Kresse, J. Furthmüller, Efficient iterative schemes for ab initio total-energy calculations using a plane-wave basis set, Physical Review B 54 (16) (1996) 11169–11186. doi:10.1103/PhysRevB.54.11169.
URL http://link.aps.org/doi/10.1103/PhysRevB.54.11169

[82] J. Heyd, G. E. Scuseria, M. Ernzerhof, Erratum: "Hybrid functionals based on a screened Coulomb potential" [J. Chem. Phys. 118, 8207 (2003)], The Journal of Chemical Physics 124 (21) (2006) 219906. doi:10.1063/1.2204597.

URL http://scitation.aip.org/content/aip/journal/jcp/124/21/10.1063/1.2204597

[83] J. P. Perdew, K. Burke, M. Ernzerhof, Generalized Gradient Approximation Made Simple- ERRATA, Physical Review Letters 77 (18) (1996) 3865–3868. doi:10.1103/PhysRevLett.77.3865.
URL http://www.ncbi.nlm.nih.gov/pubmed/22502509%5Cnhttp://www.ncbi.nlm.nih.gov/pubmed/10062328%5Cnhttp://link.aps.org/doi/10.1103/PhysRevLett.77.3865

[84] K. Burke, F. G. Cruz, K. C. Lam, Unambiguous exchange-correlation energy density, Journal of Chemical Physics 109 (19) (1998) 8161–8167. doi:10.1063/1.477479.

[85] P. E. Blöchl, O. Jepsen, O. K. Andersen, Improved tetrahedron method for Brillouin-zone integrations, Physical Review B 49 (23) (1994) 16223–16233. doi:10.1103/PhysRevB.49.16223.

[86] J. D. Pack, H. J. Monkhorst, "special points for Brillouin-zone integrations"-a reply, Physical Review B 16 (4) (1977) 1748–1749. doi:10.1103/PhysRevB.16.1748.

[87] S. Baroni, P. Giannozzi, A. Testa, Elastic Constants of Crystals from Linear-Response Theory, Physical Review Letters 59 (23) (1987) 2662–2665. doi:10.1103/PhysRevLett.59.2662.

[88] S. Baroni, S. De Gironcoli, A. Dal Corso, P. Giannozzi, Phonons and related crystal properties from density-functional perturbation theory (2001). arXiv:0012092v1, doi:10.1103/RevModPhys.73.515.

[89] X. Gonze, C. Lee, Dynamical matrices, Born effective charges, dielectric permittivity tensors, and interatomic force constants from density-functional perturbation theory, Physical Review B - Condensed Matter and Materials Physics 55 (16) (1997) 10355–10368. doi:10.1103/PhysRevB.55.10355.

[90] I. R. Shein, V. L. Kozhevnikov, A. L. Ivanovskii, First-principles calculations of the elastic and electronic properties of the cubic perovskites SrMO3 (M=Ti, V, Zr and Nb) in comparison with SrSnO3, Solid State Sciences 10 (2) (2008) 217–225. doi:10.1016/j.solidstatesciences.2007.09.013.
URL http://www.sciencedirect.com/science/article/pii/S1293255807002609

[91] A. Roldan, D. Santos-Carballal, N. H. de Leeuw, A comparative DFT study of the mechanical and electronic properties of greigite Fe ¡sub¿3¡/sub¿ S ¡sub¿4¡/sub¿ and magnetite Fe ¡sub¿3¡/sub¿ O ¡sub¿4¡/sub¿, The Journal of Chemical Physics 138 (20) (2013) 204712. doi:10.1063/1.4807614.
URL http://aip.scitation.org/doi/10.1063/1.4807614

[92] J. F. Martel, S. Jandl, B. Viana, D. Vivien, Crystal-field study of Sm 3+ ions in Sm 2 O 3, Sm 3+: Gd 2 O 3 and Sm 3+: Y 2 O 3, Journal of Physics and Chemistry of Solids 61 (9) (2000) 1455–1463.

[93] M. De Jong, W. Chen, T. Angsten, A. Jain, R. Notestine, A. Gamst, M. Sluiter, C. K. Ande, S. Van Der Zwaag, J. J. Plata, C. Toher, S. Curtarolo, G. Ceder, K. A. Persson, M. Asta, Charting the complete elastic properties of inorganic crystalline compounds, Scientific Data 2 (2015) 1–13. doi:10.1038/sdata.2015.9.

[94] W. B. W. Keramidas, V. G., Vibrational Spectra of Oxides with the C-type rare earth oxide structure, Spectrochimica Acta 28A (1971) 501–509.

[95] V. V. Afanas'ev, M. Houssa, A. Stesmans, M. M. Heyns, Band alignments in metal-oxide-silicon structures with atomic-layer deposited Al2O3 and ZrO2, Journal of Applied Physics 91 (5) (2002) 3079–3084. doi:10.1063/1.1436299.

[96] H. Yang, H. Wang, H. M. Luo, D. M. Feldmann, P. C. Dowden, R. F. DePaula, Q. X. Jia, Structural and dielectric properties of epitaxial Sm2 O3 thin films, Applied Physics Letters 92 (6) (2008) 2–5. doi:10.1063/1.2842416.

[97] S. Kaya, E. Yilmaz, H. Karacali, A. O. Cetinkaya, A. Aktag, Samarium oxide thin films deposited by reactive sputtering: Effects of sputtering power and substrate temperature on microstructure, morphology and electrical properties, Materials Science in Semiconductor Processing 33 (2015) 42–48. doi:10.1016/j.mssp.2015.01.035.
URL http://dx.doi.org/10.1016/j.mssp.2015.01.035